Advanced 3D Geophysical Imaging Technologies for Geothermal Resource Characterization

Haijiang Zhang[1,3], Erika Gasperikova[2], Beatrice Parker[1], Ari Tryggvason[5], Olafur Gudmundsson[5], Tim Seher[1], Gregory Newman[2], Michael Fehler[1], and Knutur Arnason[4]

[1]Earth Resources Laboratory, Massachusetts Institute of Technology, 7700 Mass Ave Room 54-524, Cambridge, MA 02139

[2]Lawrence Berkeley National Laboratory, 1 Cyclotron Road, MS90R1116, Berkeley, CA 94720

[3] University of Science and Technology of China, Hefei, China

[4]ISOR Iceland GeoSurvey

[5]Depth of Earth Sciences, Uppsala University, Villavägen 16, SE-75236 Uppsala, Sweden

ABSTRACT

We describe the ongoing development of joint geophysical imaging methodologies for geothermal site characterization and demonstrate their potential in two regions: Krafla volcano and associated geothermal fields in Northeastern Iceland, and Coso Hot Springs in California, USA. The Coso field is a high temperature reservoir similar to Krafla in Iceland. Each area is a locus of significant geothermal energy production. The complex geology of these sites also makes them excellent targets for developing and testing of strategies for joint imaging of magnetotelluric (MT) and micro-earthquake (MEQ) data. Our ultimate aim is to construct coupled 3D resistivity and velocity models of these geothermal systems and use them to better understand and exploit them.

INTRODUCTION

Reliable methods for exploration and characterization of geothermal reservoirs are crucial for risk reduction in geothermal drilling, and for economic operation of geothermal production sites. Various approaches employed include surface geological mapping, geochemical sampling, active or passive geophysical remote sensing, including electromagnetic and seismic techniques. Unlike other approaches, the geophysical techniques provide information about the subsurface, where borehole sampling is restricted. However, the degree to which a geophysical technique can be used to successfully infer geothermal reservoir properties (e.g. orientation and density of fractures, temperature and fluid saturation) depends on how uniquely the reservoir parameters are related to the geophysical parameters. Because these relationships are often non-unique (e.g. high brine saturation and high clay content both produce low electrical resistivity) it may be necessary to integrate multiple techniques to better interpret reservoir parameters from geophysical data (cf. Garg et al., 2007). The simplest approach of combining these methods is to seek correlations in images of the various geophysical attributes in the subsurface (i.e. velocity, density and electrical resistivity) with temperature and well log information and fluid producing intervals (cf. Newman

1

et al., 2008). More sophisticated approaches of integrating data employ joint geophysical imaging (JGI) methodologies. In this paper we describe our initial attempts to develop a JGI methodology for MEQ and MT data. These geophysical measurements are the most common employed in geothermal resource characterization studies. Here we focus our development on two high temperature geothermal systems, Krafla in Iceland and Coso in the southwestern United States.

KRAFLA GEOTHERMAL AREA

The Krafla volcanic system is located within the neo-volcanic zone in northeastern Iceland and consists of a central volcano with NNE-SSW trending fissure swarm and ESE-WNW transform graben running through it. The Krafla Geothermal plant produces 60 MW from on the average 15-17 drill holes at the time (33 holes in total). Figure 1 shows elevations in 15x15 km study area of the Krafla volcanic system along with 102 MT sounding sites (white symbols) that were used in the 3D inversion. The blue diamond indicates the location of the IDDP (Iceland Deep Drilling Program) well. MT data were acquired during 2004–2006 campaigns by several research groups.

MEQ data used in the analysis were collected from multiple networks in the Krafla area from 2004-2011. In total, there are 808 earthquakes and 69 stations used for our seismic imaging. Figure 2 shows the network and event locations.

COSO GEOTHERMAL FIELD

The Coso geothermal field is located between the eastern flank of the Sierra Nevada and the western edge of the Basin and Range tectonic province of southeastern California, and lies within the Walker Lane/Eastern California Shear Zone. The tectonics of the Coso field shows a transition between the right-lateral slip San Andreas fault-plane and the extensional tectonics of the Basin and Range province. The hot springs in the area are primarily associated with oblique faults (Roquemore, 1980). The Coso geothermal field currently produces
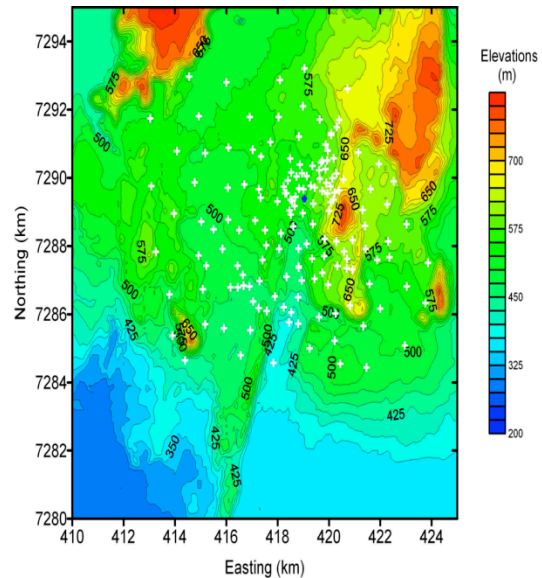

Figure 1. Krafla MT site (+) and elevation map. The IDDP well is indicated by the blue diamond at 417355 Easting and 7287655 Northing, which is Longitude -16.8, Latitude 65.7 in Figure 2, and zero in Figure 7.
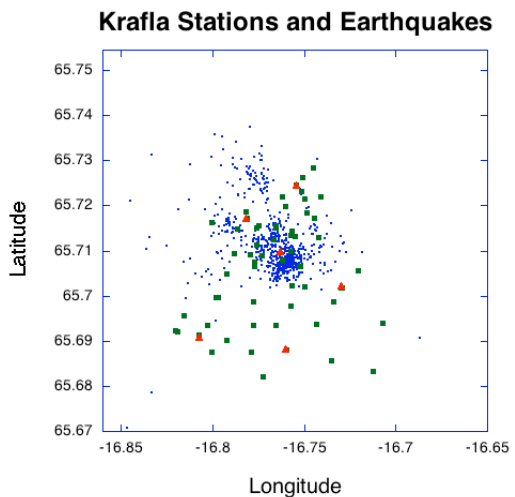

Figure 2. Krafla MEQ network observation locations (red triangles are borehole stations and green squares are surface stations) and event locations (blue dots).

nearly 300 MW of electricity from 100 wells with production depths ranging from 600 to 3700 meters. A map of the MT stations acquired over the Coso system is displayed in Figure 3 along with the topography of the study region. The MT data were acquired between 2003 and 2005. A map of the MEQ and event locations is shown in Figure 4. Wu and Lees (1999) and Lees and Wu (2000) have published results of previous analyses of Coso data using seismic tomography.
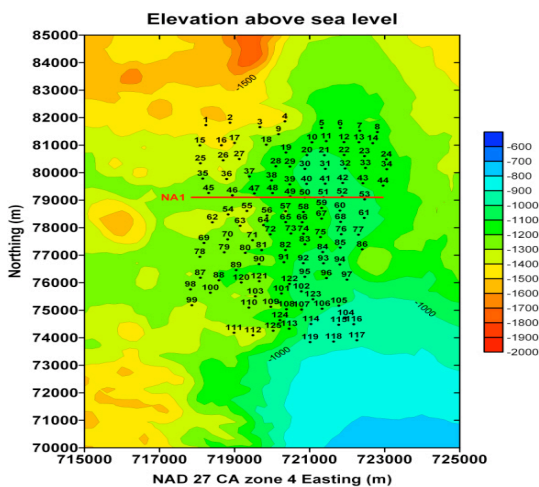

Figure 3. Coso MT site and elevation map. Line NA1 is contiguous electric field measurement line. Site 65 is at 720359 Easting and 78203 Northing, which is Longitude -117 ° 46' and Latitude 36 ° 02' in Figure 4, and (0, 0) in Figures 5 and 6.
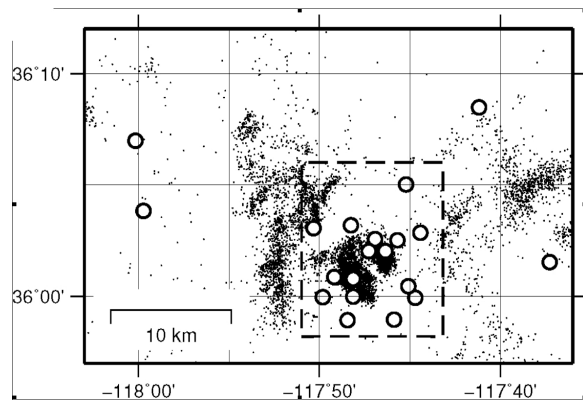

Figure 4. Coso MEQ network sites (O) and event locations. Dashed box shows region imaged using seismic tomography.

MT DATA ANALYSIS AND INVERSION

MT exploits naturally occurring, broadband electromagnetic (EM) wave fields over the Earth's surface as sources to image underground resistivity structure. The EM fields arise from regional and worldwide thunderstorm activity and from interaction of the solar wind with the Earth's magnetosphere. These EM sources are remote and the Earth has a high index of refraction relative to the overlaying atmosphere; therefore the EM waves are assumed to be planar and to propagate vertically into the Earth. The waves are arbitrarily polarized over a 3D Earth, which requires a tensor formulation, in other words a vector measurement of the EM fields, to completely represent the subsurface geoelectric structure.

The horizontal EM field spectra (Ex, Ey, Hx, Hy) are interrelated by

$$E = [Z] H \qquad (1)$$

where Z is a 2x2 impedance tensor, obtained for each MT recording station as a function of frequency. Apparent resistivity and impedance phase quantities, that are more intuitive to inspect and interpret (Vozoff, 1991), can be readily obtained by manipulating the elements of the impedance tensor off-diagonal components.

MT data were recorded for frequencies between 0.003 and 300 Hz at both geothermal fields. For inversions we used three points per decade, giving a total of 15 frequencies that were used for the inversion. Only the off-diagonal impedance matrix components were inverted, and apparent resistivity and phase calculated for xy and yx-modes. The initial starting model for Krafla was a five-layer model with a

3

resistive surface layer, a shallow low-resistivity layer, an intermediate high-resistivity, a deep low-resistivity layer, and a relatively resistive basement. This model was subsequently refined using the inversion process described below. For Coso, an initial 3D resistivity model was constructed from a series of 2D resistivity sections of the reservoir that were stitched together (Newman et al., 2008). These 2D resistivity sections were derived from inverting the transverse mode (TM) data, where it was assumed that the geological strike trends North-South.

Our ultimate aim was to construct 3D resistivity models of the geothermal systems in the studied areas and interpret them in terms of structure. To accomplish this goal we applied an inversion process, where the observed impedance data were fit in a least squares sense to model data, using the 3D starting models described above. The model data were produced by solving Maxwell's equations for 3D resistivity variations and plane wave source excitation at a discrete set of frequencies. These frequencies correspond to those used to specify the impedance tensor in the field measurements. To stabilize the inversion process, additional constraints were added such as spatial smoothing of the resistivity model. For the Krafla data set, the 3D MT inversion code (Newman and Alumbaugh, 2000) was run on 5145 cores of NERSC Cray XT4 Franklin system. Total processing time was on the order of 200 hours. Using the same code, the initial 3D analysis of Coso was first carried out in 2008 (Newman et al., 2008) on two different distributed computing systems, using 512 to 100 processor cores, with cumulative processing times of approximately several months. The 3D imaging grids employed both for Coso and Krafla used a minimum mesh size of 100 m.

SEISMIC ANALYSIS AND INVERSION

We apply the double difference tomography algorithm (Zhang and Thurber, 2003, 2006) to image the velocity models of Krafla and Coso areas. We choose a velocity node spacing of 300 m for Krafla and 500 m for Coso in all spatial dimensions.

Each tomography scheme suffers from the non-uniqueness of the inverse problem caused by insufficient sampling of portions of the model. This problem is usually addressed by introducing an additional criterion in the inverse problem. The tomography code (Zhang and Thurber, 2003, 2006) used in this study, applies a flatness constraint to the model update. The value of the flatness with respect to the starting model is constrained by two parameters - the smoothing and the damping. In this study we apply an L-curve criterion (cf. Farquharson and Oldenburg, 2004) that allows us to evaluate the trade-off between the model norm, the flatness of the velocity update, and the normalized traveltime misfit.

For the tomographic studies of the Krafla and Coso areas, we started from one-dimensional velocity models. For the Krafla area, only catalog (e.g. arrival time picked by us or an analyst) arrival times were available. We used both absolute and differential times constructed from the catalog data. For the Coso area, both catalog and waveform cross-correlation times were used. The final catalog differential travel time RMS residuals for the Krafla area was 43 ms. The final catalog differential time and cross-correlation time RMS residuals for the Coso area were 51 ms and 12 ms.

COMBINED ANALYSIS

A complex and difficult issue is how to image different geophysical data types with multiple attributes in a combined analysis. The goal of combined analysis is to find a unified model that takes advantage of the strengths of each observation and inversion methodology. One possibility is to link the attributes in the inversion process to an underlying rock physics model (saturations and rock porosity) that can be used to reliably describe the rock and reservoir formations. In situations where such information through well logs and cores is available it should be exploited. In many cases it is ambiguous, so we have adopted a different type of empirical linkage that seeks structural correlations between the different geophysical attributes - velocity and resistivity. Here it is understood that some underlying geological process is at work that causes the structural linkage. Gallardo and Meju (2003) introduced an intuitive geometrical approach using a cross gradient function to enforce structural similarity. While enforcing structural similarity has appeal, there is the distinct possibility that the different geophysical attributes are not structurally coupled at all, so a biased image would result from the analysis. The possibility of obtaining a biased image is an example of the difficulties in a combined analysis. A simple comparison of uncoupled velocity and resistivity images can be indicative of whether a structurally coupled inversion is reasonable. In the case of Coso, some striking similarities in the attributes are observed (Figures 5 and 6). However, because of different model resolutions and uncertainties, there exist evident structure dissimilarity between velocity and resistivity models, which can be seen from the scatter points in the cross plot of two attributes. For Krafla, because of the difference in model sizes, the case is not as clear, but over a subset of the image volume, some structural linkage also appears plausible (Figure 7).
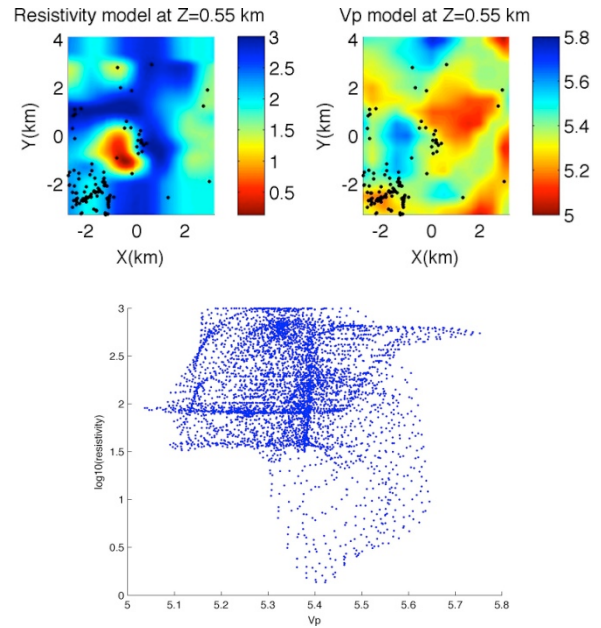

Figure 5. Maps showing log electrical resistivity and P-wave velocity images at 0.55 km below sea level obtained through separate inversion of MT (top left) and seismic (top right) data from Coso, with a scatter cross plot shown at bottom. Cross plot shows results from throughout the respective image volumes. Although some regions are clearly correlated, the structures of the two models show some dissimilarity. Earthquake locations within +-0.2 km of 0.5 5km are indicated by black dots in the resistivity and velocity models.

CONSIDERATIONS FOR JOINT INVERSION

Other issues to consider when coupling the velocity and resistivity attributes through joint inversion are grid alignment, mesh size, and the differing resolution and uncertainties between the different data sets. These issues raise important questions in setting up a joint imaging frame work for common structure.

Some choices need to be made to deal with these issues. Resolution for MT measurements will be determined by the spatial coverage of the measurement sites

and the sounding frequencies. For the MEQ, data resolution will be determined by the number of earthquakes, their spatial distribution, the frequency content of the seismic data, and the aperture of the seismic network. Ideally, resolution between the two measurements will be similar. However, the number and location of seismic events dictate the size of the mesh that can be employed for velocity imaging. For both the Coso and Krafla MEQ data sets the cells used in the meshing was 3 to five times larger than those used for the MT data sets. Velocity images thus obtained are interpolated to correspond to the finer meshing used to image resistivity. Using a finer mesh for constructing the velocity images directly was not feasible because the velocity of many of the smaller cells will not be updated during the inversion.
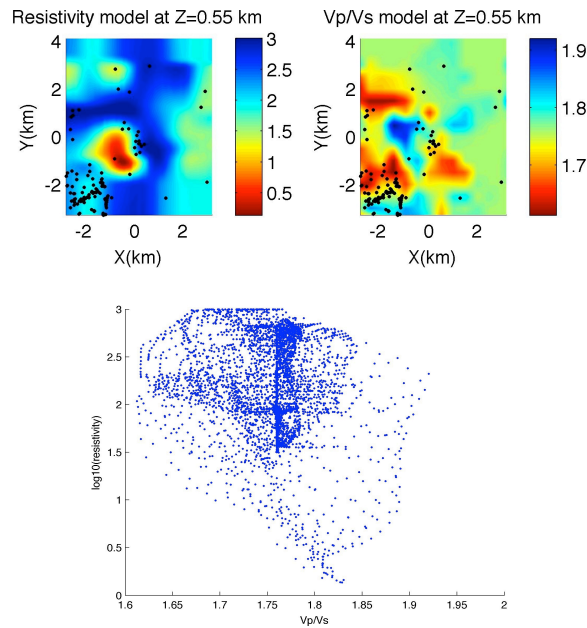

Figure 6. Maps showing log electrical resistivity and Vp/Vs velocity ratio images at 0.55 km below sea level obtained through separate inversion of MT (top left) and seismic (top right) data from Coso, with a scatter cross plot shown at bottom. Cross plot shows results from throughout the respective image volumes. Although some regions are clearly correlated, the structures of two models show some dissimilarity.
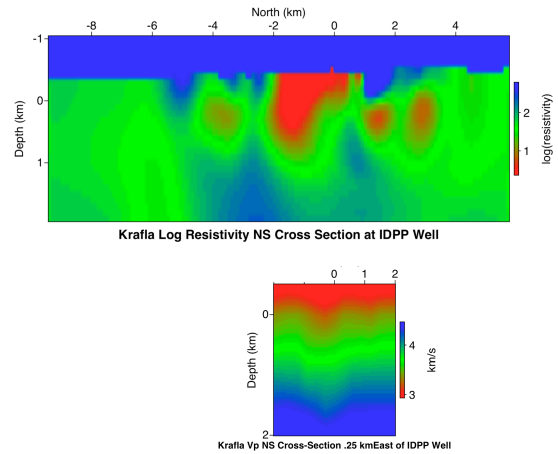

Figure 7. Comparison of electrical conductivity and velocity images (Vp) at Krafla obtained through separate inversion of seismic and MT data. Because of limited aperture caused mainly by the relatively small zone of seismicity, the velocity can only be imaged over a subset of the conductivity imaging volume. The velocity profile is 0.25km east of the IDPP well. The coordinate center is at the IDPP well (latitude 65.715891, longitude -16.764522).

Only cells intersected by MEQ ray paths can be updated in the inversion process. Another approach is to coarsen the resistivity mesh so that it is similar to the mesh used to image velocity. Currently we are exploring both approaches in designing an imaging framework to find a common structure. In either case a coordinate mapping needs to be established that interpolates specific attributes to different mesh sizes, so that the common structure constraint can be enforced.

IMPLEMENTATION

Since the geophysical properties of the subsurface can vary in any spatial direction (x, y, z), changes at any position of a particular property can be characterized in terms of intensity (magnitude) and the spatial gradient of the change in property. These ideas can be represented mathematically by vector fields of the gradients of the properties, from which it is

possible to define a structural similarity constraint. For example, Gallardo and Meju (2003) quantify the structural similarity using a cross product of the conductivity(inverse of resistivity) and velocity gradients by

$$t_{ov} = \nabla m_\sigma (x, y, z) \times \nabla m_v (x, y, z) \qquad (2)$$

where $\nabla m_\sigma (x, y, z)$ and $\nabla m_v (x, y, z)$ are the electric conductivity and seismic velocity gradients respectively; the velocity can be P-velocity, S-velocity or the ratio of P to S velocities. Upon discretization, the functions m_σ and m_v are approximated as piecewise constant across n cells representing the imaging domain. The 3D conductivity and velocity images are deemed to be structurally identical if t_{ov} vanishes everywhere. It is also possible to enforce a structural similarity between P and S wave velocity models.

In one implementation we are considering, we image seismic and MT data separately. Structural similarity is enforced as a prior constraint on either the velocity or resistivity attribute. Here we formulate an objective function

$$\phi = \tfrac{1}{2}\{\mathbf{D}(\mathbf{d}^p - \mathbf{d}^{obs})^{\mathbf{T}}\{\mathbf{D}(\mathbf{d}^p - \mathbf{d}^{obs})\} +$$

$$\tfrac{1}{2}\lambda\{\mathbf{Wm}\}^{\mathbf{T}}\{\mathbf{Wm}\} + \beta \sum_{i=1}^{n} t_{ov}^{i} \cdot t_{ov}^{i} \quad (3)$$

The active data $\mathbf{d}$ (observed or predicted denoted by superscripts *obs* and *p* respectively), weight $\mathbf{D}$ and attribute $\mathbf{m}$ corresponds to either the resistivity or velocity, with the other fixed. The factor β is a design parameter used to enforce the structural similarity constraint to acceptable tolerance. At large values of β structural similarity is better satisfied than for smaller values, but at the expense of an increase in the misfit between predicted and observed data. Minimization of (3) is carried out using

a variety of methods employed in geophysical inversion, depending upon the data and model types for MT and MEQ inversion (Newman and Alumbaugh, 2000; Zhang and Thurber, 2003, 2006).

Another approach we consider is to update the attributes for common structure using a joint inversion strategy of Gallardo (2007). In an inner iteration cycle the attributes are driven to have similar structure, without regard to reducing the data errors between measured and predicted data. An outer iteration loop is used to enforce acceptable fits to the respective data measurements, independent of other measurements and attributes. A flowchart illustrating this approach is shown in Figure 8.
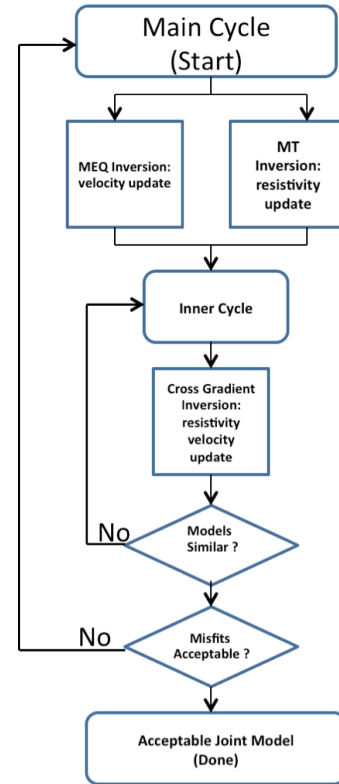

Figure 8.The joint inversion flow chart strategy from Gallardo (2007).

RESULTS

We have implemented the approach of JGI based on equation (3) for the Coso area (Figure 9). In the implementation, the resistivity model from MT imaging is used as a constraint for the velocity models through the cross-gradient constraint during the seismic velocity tomography. The resistivity model is kept fixed during the inversion, but the velocity models are updated to fit both travel time data and the structure of the resistivity model. Obviously there is a trade-off between fitting the data and finding similar structural models. The optimal parameter of β is selected through a trade-off analysis such that the velocity models fit data and structure equally well. For the Coso area, the new velocity models from the coupled inversion fit the catalog arrival times at a comparable level as the separate inversion, but the data fitting for the cross-correlation times is 20% worse (16 ms versus 13 ms). This is because at the later stage of velocity tomography, the cross-correlation times dominate the inversion system with higher weighting. Comparing the new Vp model to the resistivity model, it can be seen that the two models have more similar structures, which are reflected by the tighter and more concentrated points in the cross plot of the two attributes (Figure 9). Specifically, the high resistivity ring around the low resistivity anomaly corresponds well to the low velocity anomaly.

Newman et al. (2008) discussed the significance of the 3D resistivity model with respect to geothermal system at Coso. A classic MT response of a high temperature system is observed. A conductive argillic (smectite clay) hydrothermal alteration zone sits above and adjacent to more resistive propylitic alteration (illite clays) in the reservoir. The conductive clay cap shows at its apex diagnostic fumarole activity. The resistivity model also confirmed that faulting strongly controls the geological structure and geothermal production at Coso. These faults act as hydrological barriers to fluid flow, compartmentalizing zones where fluids can be exploited and targeted for drilling. A key feature of the resistivity model is the low-resistivity intrusive feature, seen clearly in Figures 5, 6, and 9. The feature is bounded and controlled by faulting.

Drilling showed the anomaly to be extremely hot (> 250 °C), with the well losing circulation in a highly fractured region of the rock, but no fluids were encountered. This feature's low resistivity could not be ascribed to conductive clays because of its high temperature. Instead it was surmised that the low resistivity arises from large sets of fluid bearing fractures, perhaps brines, located away from the drill stem.
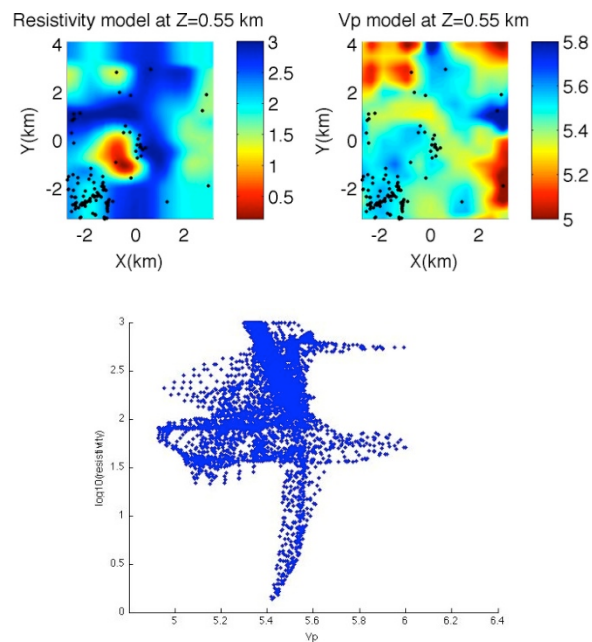

Figure 9. Comparison of electrical resistivity and Vp images at Coso obtained using JGI. Images at 0.55 km below the sea level are shown (top), with cross plot at bottom. The structures of two models now show significantly more similarity than obtained with inversion of individual data sets.

Using a common structure constraint to image velocity in Figure 9 is quite reasonable because of the observation that faulting strongly controls placement of the intrusive resistivity anomaly and fluid production at Coso (Newman et al., 2008). The relatively higher velocity observed in the zone of low resistivity in the SW portion of the model may be indicative of the presence of fluid filled fractures. This low resistivity and high velocity anomaly is also associated with high Vp/Vs ratio (> 1.8) determined in this study (Figure 6) as well as by Lees and Wu (2000), which is common for fluid-filled fractures. This example shows that by using multiple geophysical attributes, it is possible to alleviate some ambiguity in interpretation. Interpretation of the low velocity feature ringing the intrusion is more difficult to explain. This area corresponds to enhanced resistivity within the reservoir due to high temperature hydrothermal alteration of clay products. The Vp/Vs model in Figure 6 shows low Vp/Vs anomalies (<1.7) associated with this ring. We hypothesize that this ring may be concentrated with steams due to high temperatures and drop in reservoir pressures as the field is produced, which would cause low Vp and low Vp/Vs. Generally speaking higher velocity corresponds to presence of fluids. The is clearly the case in the Devil's Kitchen area (Y=0 and X< -2 km in Figure 7) and the locust of production activity in the southwest corner of the field (see lower left hand corner of the velocity and resistivity images in Figure 9. This area is also associated with seismicity due to reinjection activities. When imaged without constraints, this region's velocity was shown to be low, not indicative of fluids (Figure 5). The cross plot of resistivity and velocity in Figure 9 suggests usefulness of the JGI approach. Several clusters or regions with different relationship between resistivities and velocities could be identified, and suggest different sensitivities of resistivity and velocity to different geology in such a complicated geothermal system as Coso.

Currently we are carrying out JGI experiments using this and the other strategies mentioned above. For example, we will use the velocity model as a constraint for the MT inversion and see how this affects data fitting. Detailed results will be discussed at the 2012 Annual GRC meeting in the fall.

REFERENCES

Farquharson and Oldenburg, 2004, A comparison of automatic techniques for estimating the regularization parameter in nonlinear inverse problems, Geophysical Journal International, 156, 411-425.

Gallardo L. A., and Meju, M. A., 2003, Characterization of heterogeneous near-surface materials by joint 2D inversion of dc resistivity and seismic data. Geophysical Research Letters, 30, 1658, doi:1610.1029/2003/GL017370.

Gallardo, L. A., 2007, Multiple cross-gradient joint inversion for geophysical imaging. Geophysical Research Letters, 34, L19301, doi:19310.11029/12007GL030409.

Garg S. K., Prichett, J. W., Wannamaker, P. E., Combs, J., 2007, Characterization of geothermal reservoirs with electrical surveys: Beowawe geothermal field. Geothermics 36, 487-517.

Lees, J. & Wu, H., 200, Poisson's ratio and porosity at Coso geothermal area, California J. Volc. Geoth. Res., Elsevier, 95, 157-173.

Newman G. A., and Alumbaugh, D. L., 2000, Three-dimensional magnetotelluric

inversion using non-linear conjugate gradients. Geophysical Journal International, 140, 410-424.

Newman G. A., Gasperikova, E., Hoversten, G. M., and Wannamaker P. E., 2008, Three-dimensional magnetotelluric characterization of the Coso geothermal field. Geothermics, 37, 369-399.

Roquemore, G., 1980, Structure, tectonics, and stress field of the Coso Range, Inyo County, California. Journal of Geophysical Research, 85, 2434-2440, doi: 10.1029/JB085iB05p02434.

Vozoff, K., 1991, The magnetotelluric method. In: Nabighian, M.N. (Ed.), Electromagnetic Methods in Applied Geophysics, vol. 2B. Soc. Explor. Geophys., Tulsa, OK, USA, pp. 641-711.

Wu, H. & Lees, J. Three-dimensional P and S wave velocity structures of the Coso Geothermal Area, California, from microseismic travel time data J. Geophy. Res., 1999, 104, 13,217-13,233

Zhang, H., and Thurber, C. H., 2003, Double-Difference Tomography: The Method and Its Application to the Hayward Fault, California, Bull. Seism. Soc. Am, 93, 1875-1889.

Zhang, H., and Thurber C., 2006, Development and applications of double-difference tomography, Pure and Applied Geophys., 163, 373-403, doi:10.1007/s00024-005-0021-y.

ACKNOWLEDGEMENTS